Comparison analysis of five waveform decomposition algorithms for the airborne LiDAR echo signal

Guoqing Zhou, Senior Member, IEEE, Shuhua Long, Jiasheng Xu, Xiang Zhou, Bo Song, Ronghua Deng, Cheng Wang

Abstract—**The information from the components obtained by waveform decomposition is usually used to inverse topography, and classify tree species, etc. Many efforts on waveform decomposition algorithms have been presented, but are lack of comparison analysis and evaluation. Thereby, this paper compares and analyzes the performance of five waveform decomposition algorithms, Gaussian, Adaptive Gaussian, Weibull, Richardson-Lucy (RL), and Gold under different topographic conditions such as forests, glaciers, lakes, and residential areas. The experimental results reveal that (1) the Gaussian algorithm causes the biggest fitting error at 9.96 mV in forested area. It is easy to identify multiple dense peaks as single peaks. (2) There are many misjudged, superimposed, and overlapped waveform components separated by the Weibull algorithm. The Adaptive Gaussian is more capable of fitting complex waveforms, but has 122 more outliers than the Weibull algorithm does. (3) The Gold and RL algorithms decompose the largest number of waveform components (272.2k and 265.9k) in forested area; both RL and Gold algorithms can effectively improve the separability of peaks. (4) The RL algorithm is only more effective for the area with sparse vegetation than the Gold algorithm does, i.e., the Gold algorithm is capable of processing data with dense vegetation areas at a lowest false component detection rate of 1.3%, 0.9%, 1.1%, and 0.1% in four areas. (5) The Gaussian and Gold algorithms have much faster decomposition speed at 1,000/s and 2,000/s than the other three algorithms do. These results are useful for selecting different algorithms under different environments.**

Index Terms—**airborne LiDAR, waveform decomposition, Gaussian, deconvolution, Gold.**

I. INTRODUCTION

CURRENTLY, airborne LiDAR is widely used in distance measurement, vegetation monitoring, urban modeling, and marine mapping [1]-[5]. The pulse width and amplitude change when the laser beams encounter objectives of different heights. The echo signal is usually a superposition of multiple pulses as well as the sum of various noises. Therefore, a decomposition method is needed to denoise and decompose the echo signal [6].

By analyzing the amplitude, width, and other characteristics of the decomposed waveform, the geometric structure, physical characteristics, and vertical distribution of the objectives illuminated by the laser pulse can be obtained [7]. For example, the distance or height of the objective can be calculated by using the position of the waveform peaks [8]; the amplitudes of the peaks can be used as a reference for filtering out the point from the ground [9], etc.

There are two main types of algorithms used to decompose LiDAR waveforms: mathematical simulation and deconvolution. The former usually assumes that the LiDAR pulses and the backscattering cross-section of the scatterer approximates the Gaussian distribution [10]. Therefore, many mathematical simulation algorithms are based on the Gaussian distribution. For example, Wagner et al. first proposed and implemented a method based on the Gaussian functions for small-footprint airborne laser scanning (ALS) data in 2006 [11]. Chauve et al. used the generalized Gaussian functions (including logarithmic and Adaptive Gaussian functions) as kernel functions for waveform decomposition in 2007 [12]. However, since the echo signal was not modeled well enough, the error for the extracted information was relatively large. In 2017, Bruggisser et al. used the Skew Normal Distribution (SND) as a kernel function to implement waveform decomposition for the data in forested areas [13]. In 2017, Zhou et al. applied the Weibull function to the decomposition of full-waveform LiDAR data and found that the fitting model was flexible enough to simulate simple or complex waveforms [14]. However, the fit was poor and the convergence was slow when the waveform was complex.

The mathematical simulation algorithm does not take into account the interference of the LiDAR detector and system to the waveform, which also leads to the loss of the objective information. To reduce the unnecessary system effects and restore the true distribution of objectives, a second algorithm, the deconvolution algorithm, is developed. In 2010, Zhu et al. first implemented the Gold algorithm for processing ALS full-

waveform data. They heralded its great potential in processing LiDAR data [15]. In 2011, Roncat et al. addressed the inherent pathological problem of deconvolution algorithms and refitted the waveform using B-spline assisted deconvolution algorithm. The fit provided backscattered cross-sections for different objectives to be measured [16]. However, the computational complexity of B-spline processing was greatly increased, and the characteristics of waveforms were easy to be lost. In 2011, Wu et al. validated three algorithms of Non-negative least squares [17], Wiener filtering [18], and Richardson-Lucy (RL) [19]. The RL deconvolution algorithm was concluded to be the best. However, from Zhou's experiments in 2017, it was known that the RL algorithm suffers from slow convergence and poor fitting accuracy in densely vegetated areas [10]. Other published studies have successfully applied different deconvolution algorithms, such as the Sparse Constrained Regularization algorithm [20] and Bayesian Inference [21], to recover the true cross-sections of the objectives.

In recent years, a large number of waveform decomposition algorithms have emerged, but there are a few comparative experiments available that are based on real application data, such as Parrish et al. based on laboratory measuring data [22]; Wagner et al. [23], Xiu et al. [24], and Wang et al. [25] based on simulated data. Therefore, we choose some algorithms for comparative analysis. We first consider the selection of algorithms that have been successfully applied by scholars to the processing of real application data. Therefore, a few classical, improved, and frequently-used algorithms in recent years, as well as representative algorithms in the two major categories are selected. Finally, the Gaussian, Adaptive Gaussian, Weibull, Richardson-Lucy and Gold, were selected. Comparative analysis is performed under different environmental characteristics to derive their advantages and limitations.

II. Five Waveform Decomposition Algorithms

A. Basic Principles of Waveform Decomposition

The waveform decomposition is done by treating the echo signals as a combination of different object reflections within the laser spot. The objects with different spatial distribution are extracted from the reflected signals, to locate and identify the objects. Therefore, the waveform decomposition is considered as a superposition of several waveform components [8], and the
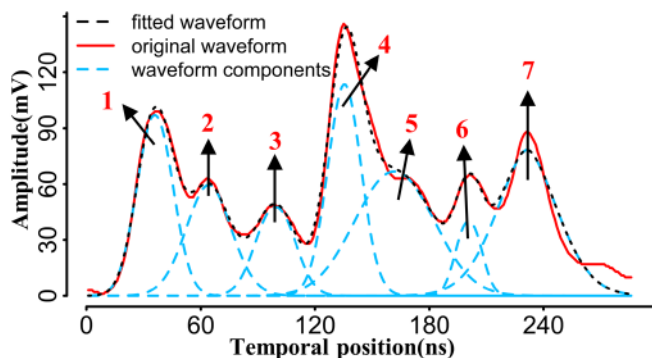

Fig. 1. Waveform component obtained from waveform decomposition.

original echo signal is fitted using an appropriate functional model. Fig. 1 shows the results of waveform decomposition, with the blue components indicating the specific time position, intensity, and width. Through the analysis of the components, information about the objective characteristics can be obtained. There are two main steps in the waveform decomposition: 1) estimation of the initial parameters; 2) optimization of the parameters and fitting the waveform.

The initial parameter estimation is a very important aspect of the waveform decomposition. Its purpose is to determine the number of effective echoes and the initial values that needed to accurately fit objective functions [26]. The existing parameter estimation methods include the Peak method, Gravity method, and Inflection Point method [27]. In order to detect hidden peaks better, this paper uses quadratic detection to estimate the initial parameters and the number of peaks (waveform components), as suggested by Wagner et al [23]. It is done by first using the over-zero point of the first-order derivative to detect the peaks [28]. The estimation of the initial parameters determines the initial value of the fitted function. Parameter optimization can be achieved by minimizing the error between the echo signal and the fitted signal. The first fit is performed using nonlinear least squares after detecting the peaks. The quality of the fit is assessed by the following equation:

$$\xi = \frac{1}{N-p} \sum_{k=1}^{N} (y_k - f(x_k))^2 \qquad (1)$$

where $\sum_{k=1}^{N} (y_k - f(x_k))^2$ is the sum of the residuals between the observed waveform and the fitting function, N is the number of samples, and p is the fitting parameter?

For complex waveforms, more precise peak detection is required. For example, when two overlapping echoes are very close, only one maximum value is detected but there are three inflection points (rather than two inflection points of a standard laser pulse). Our solution is to perform a second pulse detection of the difference between the observed waveform and the previous fit. If a peak is detected, the fit is refitted using the new component. The resulting ξ value is compared to the previous one and this procedure is repeated until the ξ value stops decreasing. The iterations for parameter optimization end if the difference of RMSEs (root mean square errors) between the observed and the fitted data is three times less than the standard deviation of the mean noise [18], [29]. The mean noise is estimated for every return waveform at all sampling points of a waveform. If the estimated waveform amplitude is less than three times the standard deviation of the mean noise, the waveform component is considered false and will be rejected [8], [22], [30]. The signal can be fitted on this basis using the following different algorithms.

B. Gaussian Algorithm

The Gaussian algorithm was first proposed by Wagner et al [11]. They demonstrated the validity of decomposing the waveform using the Gaussian function as a kernel function through radar equation [11]. The basic idea is to use the Gaussian model with a shape similar to the laser pulse to fit the echo signal. The analytic expression for the Gaussian function

can be written as:

$$f(x) = \sum_{j=1}^{n} A_j exp\left(-\frac{(x-\mu_j)^2}{2\delta_j^2}\right) \qquad (2)$$

where n is the number of waveform components, A_j, μ_j, and δ_j are the amplitude, peak position, and standard deviation of the j-th waveform component respectively.

C. Adaptive Gaussian Algorithm

Considering that the Gaussian algorithm may not be suitable for fitting complex waveforms, Chauve et al. were the first to propose the use of a generalized Gaussian function (Adaptive Gaussian) to fit the echo signal [12]. The basic idea is to introduce another variable (also known as rate parameter) to minimize the residuals of the model. The Adaptive Gaussian function can simulate a sharper or flatter Gaussian shape when the rate parameter takes on a different interval. This allows the component to reproduce the actual waveform more accurately. The expression for the Adaptive Gaussian algorithm can be written as:

$$f_{AG}(x,\theta) = \sum_{j=1}^{n} A_i exp\left(-\frac{(x-\mu_j)^{\lambda}}{2\delta_j^2}\right) \qquad (3)$$

The rate parameter λ in Equation (2) (Gaussian) is 2, but the rate parameter λ in Adaptive Gaussian is more flexible than that in Gaussian.

D. Weibull Algorithm

The Weibull function is a failure distribution function derived from statistical theory by Weibull [31]. It was first applied to image processing for the Synthetic Aperture Radar (SAR) by Tison et al. [31]. Its basic idea is to fit symmetric or asymmetric peaks using a function containing four parameters. Its function can be written as:

$$f_W(x,\theta) = \sum_{i=1}^{n} A_i \frac{k}{\delta_i}\left(\frac{x-\mu_i}{\delta_i}\right)^{k-1} exp\left(\left(-\frac{x-\mu_i}{\delta_i}\right)^k\right) \qquad (4)$$

where A_j is the magnitude, μ_j is the position parameter, k (>0) is the shape parameter, and δ_i is the scale parameter. The shape parameter k captures the asymmetry or skewness of the waveform, overcoming the disadvantage that the Gaussian function only applies to symmetric distributions.

E. Richardson-Lucy Algorithm

The Richardson-Lucy (RL) algorithm is a nonlinear iterative algorithm developed by Richardson and Lucy [32]. It was originally used to rebuild astronomical images. Its basic idea is to maximize the likelihood of the recovered image by using an Expectation Maximization algorithm [33]. When the waveform profile of a LiDAR echo signal is viewed as a $1 \times N$ image [19], the convolution of the t-th iteration solution is as follows:

$$P_{t+1}(x) = P_t(x) \cdot \left(\frac{P(x)}{(P_t * R)(x)} * R(x)\right) \qquad (5)$$

where $*$ is the convolutional operation, $P(x)$ is the observed value at position x, $P_t(x)$ is the most probable value, and $R(x)$ is the point spread function. The residual of each iteration is

calculated by the following equation:

$$\gamma_t(x) = P(x) - (P_t * R)(x) \qquad (6)$$

The residual will converge as the iteration progresses. The iteration can be terminated by selecting a specific residual threshold or by setting a constant number.

F. Gold Algorithm

The Gold algorithm is a non-oscillatory, stable deconvolution algorithm, pioneered by Zhu et al. for processing small-footprint LiDAR data [15]. The solution of the Gold algorithm is always non-negative [34], an important property applicable to waveform decomposition. The Gold algorithm has been successfully applied to the decomposition of multiple peaks in γ-ray spectroscopy [34]. For the deconvolution of discrete data, it is solved by iterating on the following equation:

$$y(i) = \sum_{k=0}^{n-1} h(i-k)x(k), i = 0,1,2,\dots,n\text{-}1 \qquad (7)$$

where $h(i)$ is the impulse response function, x and y are the input and output vectors respectively, n is the sampling number of vector h, i is the i-th sampling point, and $x(k)$ is the differential backscattering cross-section of the k-th waveform. After matrix transformation, the Gold function can be expressed as the following equation [35]:

$$X^{(n)}(i) = \frac{X^{(n-1)}(i)}{\sum_{j=1}^{m} h(i-j)X^{(n-1)}(j)} X^{(n)}(i) \qquad (8)$$

For the deconvolution algorithms Gold and RL mentioned above, the system impulse response, and output pulses must be known to deconvolute the echo signal [36].

III. STUDY SITES AND LIDAR DATA

A. Study Sites

Combining different geographies, ecoregions, and varying numbers of routes, the following study sites were selected to test the robustness of different algorithms in processing full-waveform LiDAR data. As shown in Fig. 2: (1) Yellowknife (Fig. 2a), the capital of the Northwest Territories of Canada, which is flat with sparse vegetation, mainly birch and spruce [37]. There are also many outcrops of rock. The 24,366 sets of waveform samples were intercepted for the experiment. (2) Ogooué province (Fig. 2b), which belongs to the Gabonese Republic, is located on the west coast of central Africa. The region is dotted with dense rainforest vegetation, including African mahogany and a variety of mahogany trees with high biodiversity [38]. A flight line over Ogooué province was selected and 62,456 sets of waveform data were cropped for experiment. (3) Louisiana State (Fig. 2c), this state is located in the southern part of the United States with low and flat terrain. There are many residential and commercial buildings in this area with a dense population. The trees are mainly pine and cypress. More information can be found in [39]. A flight line that flew over the city was selected, with which 30,518 sets of the waveform data were extracted for experiment in this paper. (4) Larsen Harbor (Fig. 2d), a seaport in Antarctica, at the southeastern tip of South Georgia. The area is covered by an ice sheet with an average thickness of about 1.9 km [40]. 42,861

sets of waveform samples were collected from a single flight line for waveform decomposition. These four areas including sparse and dense vegetation are suitable for comparing and testing the performance of different LiDAR waveform decomposition algorithms.

LiDAR data were collected via the NASA Goddard Space Flight Center Airborne Observation Platform (https://lvis.gsfc.nasa.gov). The platform is equipped with the Hyperspectral Imaging Spectrometer, Land, Vegetation, and Ice Sensor (LVIS). The full waveform data sets for the above four regions were acquired using a LiDAR system with 1,064 nm pulsed laser [41]. The average flight altitude of the NASA aircraft is 1,000 m above the ground. At this altitude, the ground spot size is about 25 cm. The laser emits at a frequency of up to 400,000 Hz with about 1-4 waveforms per square meter. The waveforms store the echoes in digital form, each with 16-bit intensity information which can be assumed to be the amplitude of a waveform. The data set for Larsen Harbor was collected on September 26, 2015. 700,000 waveform data were collected in the flight line, and each waveform is split into 528-time bins with 1 ns interval. The data set for Yellowknife was collected on July 12, 2019. The flight line contains 350,000 waveform data, and each waveform is split into 1,216-time bins with 1 ns interval. The data set for Ogooué was collected on February 20, 2016, and the data set for Louisiana was collected on May 23,

2019. Both regions contain 400,000 waveforms for the selected flight lines, each waveform being split into 1,024-time bins with 1 ns interval. More information can be found in [42].

B. Data Pre-processing

The LiDAR echo signals are affected by factors such as the environment and LiDAR system [43], [44]. As a result, the echo signals are often mixed with environmental noise. The noise makes the objective information reflected by the LiDAR pulse inaccurate or even maps out information that does not exist. Generally, the noise manifests itself as a small amount of jitter in the waveform curve. However, it can cause a lot of interference to the subsequent waveform decomposition. Therefore, denoising is a prerequisite for waveform decomposition. Before the waveform decomposition, all waveform data are pre-processed by MATLAB (https://www.mathworks.com/) with steps such as threshold denoising and mean filtering. The detailed description for denoising LiDAR data can be referenced to our previous publication, i.e., Long et al. [45]. Then the waveform decomposition of the data was performed via the R language (https://www.r-project.org/) [46], [47]. The LVIS system records the mean noise value of each waveform sample in real-time, which is very helpful for denoising. The following experiments are based on a good denoising effect.
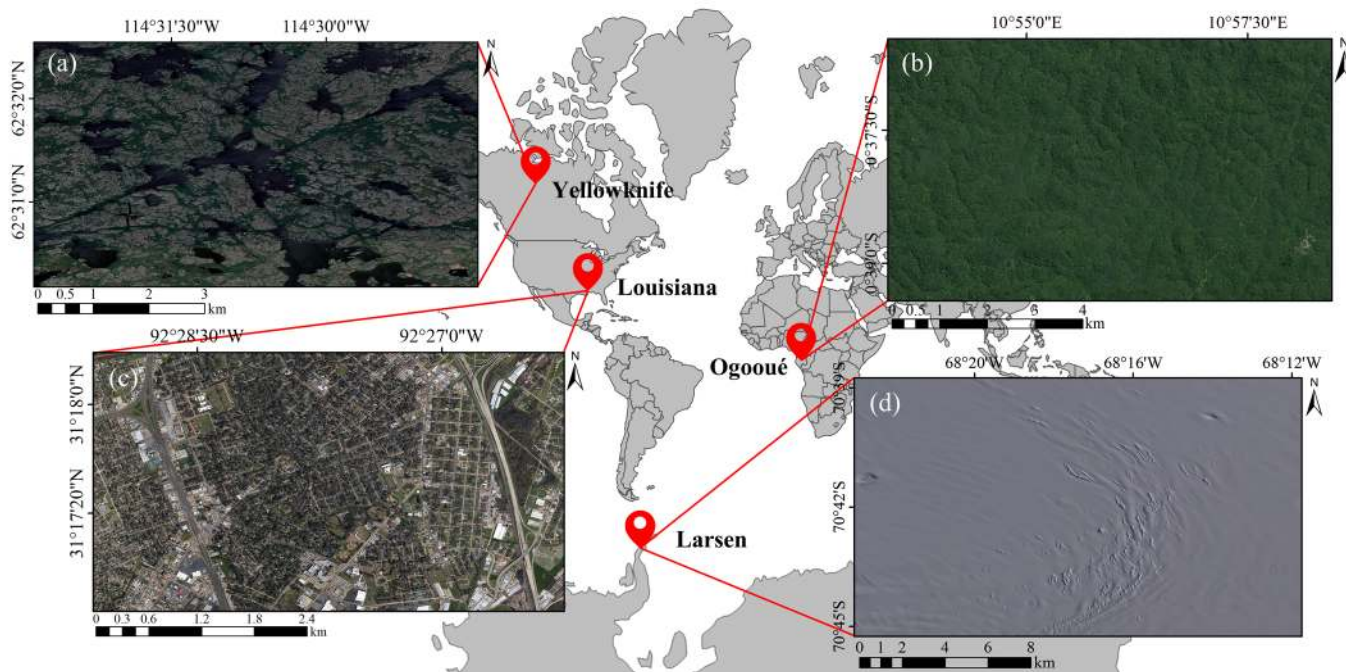

Fig. 2. Location of LiDAR echo datasets in four regions of Yellowknife, Ogooué, Louisiana, and Larsen Harbor.

IV. Results And Discussion

A. Comparison Analysis of the Number of Components

In order to effectively evaluate the performance of the five algorithms, Table I lists the results when using different numbers of waveform components. The method proposed by Parrish et al. [22] is adopted to eliminate the effect caused by

the noise to the decomposition accuracy, i.e., the waveform component is considered false, if the estimated waveform amplitude is three times less than the standard deviation of the mean noise. As observed from Table I, the following conclusions can be drawn up:

1) The Gold algorithm can produce the largest number of waveform components (272.2k) and the Gaussian algorithm the lowest (125.4k) among the five algorithms in the Ogooué area.

Similar results are obtained in the Yellowknife area. This result indicates that the Gold algorithm has a strong decomposition ability, especially in the case of multiple echoes in forested areas. However, the RL algorithm decomposes the number of components (55.6k) more than the Gold algorithm (53.0k) in the ice-covered region of Larsen Harbor. These results indicate that the RL algorithm has a better decomposition performance than the Gold algorithm does in the region with simple echoes.

2) The Gaussian, Adaptive Gaussian, Weibull, and RL algorithms have 13.7%, 4.7%, 6.5%, and 3.8% probability of detecting false components in the Ogooué region, respectively. However, the Gold algorithm significantly reduces the false components detection rate to 1.3%. The number of waveform components retrieved by the Weibull algorithm decomposition (189.7k) is similar to that retrieved by the Adaptive Gaussian (198.6k), but the Adaptive Gaussian algorithm is more successful in decomposing the waveform components than the Weibull algorithm does.

3) The Adaptive Gaussian algorithm decomposes the waveform into 1 to 4 waveform components at 47.7k from the Louisiana data, which is more than the RL (38.1k) and Gold (38.5k) algorithms do; the Adaptive Gaussian algorithm decomposes the waveform into 5 to 8 components at 8.2k, which is much less than that by both RL (42.3k) and Gold algorithms (43.6k). These results indicate that both RL and Gold algorithms have a high ability in the detection of hidden peaks.

TABLE I
THE NUMBER OF DECOMPOSED COMPONENTS OBTAINED BY THE FIVE ALGORITHMS FOR FOUR REGIONS OF OGOOUÉ, LOUISIANA, YELLOWKNIFE, AND LARSEN HARBOR

	Number of components	1-2	3-4	5-6	7-8	9-10	11-12	13-14	False	Total	Effective
Ogooué	Gaussian	42,895	54,098	23,745	4,207	439	33	0	**17,182**	**125,417**	108,235
	Adaptive Gaussian	44,715	80,307	51,551	17,272	3,830	695	201	9,333	**198,571**	189,238
	Weibull	43,666	76,151	49,244	16,515	3,513	578	28	12,330	**189,695**	177,365
	RL	28,902	70,026	78,856	54,846	25,019	6,942	1,320	10,105	265,911	255,806
	Gold	28,692	73,320	81,285	56,507	24,940	6,624	844	**3,539**	272,212	268,673
Louisiana	Gaussian	22,534	8,619	1,926	344	37	0	0	2,476	33,460	30,984
	Adaptive Gaussian	**30,532**	**17,187**	**6,473**	**1,671**	259	33	0	1,179	56,155	54,976
	Weibull	29,806	16,128	6,243	1,641	241	22	0	2,488	54,081	51,593
	RL	18,798	19,317	23,221	19,078	10,862	4,190	1,180	3,769	96,646	92,877
	Gold	**19,470**	**19,003**	**23,735**	**19,930**	10,181	2,536	318	857	95,173	94,316
Yellowknife	Gaussian	21,141	969	213	21	0	0	0	470	22,344	21,874
	Adaptive Gaussian	24,272	2,373	1,046	199	27	0	0	419	**27,917**	27,498
	Weibull	23,708	1,857	933	156	27	0	0	788	26,681	25,893
	RL	23,846	2,282	1,314	220	0	0	0	249	27,662	27,413
	Gold	24,015	2,268	1,425	225	9	0	0	272	27,942	27,670
Larsen	Gaussian	43,952	2,027	137	0	0	0	0	738	46,116	45,378
	Adaptive Gaussian	45,283	4,250	684	101	18	0	0	634	50,336	49,702
	Weibull	45,099	4,132	653	94	18	0	0	1,669	49,996	48,327
	RL	43,680	8,786	2,454	563	102	0	0	56	**55,585**	55,529
	Gold	44,536	6,667	1,525	212	9	0	0	27	**52,949**	52,922

B. Comparison Analysis of the Component Position

To further explore the characteristics of the five algorithms, the samples including simple and complex waveforms are selected to represent the differences between the original signals and the fitted signals. Their results are shown in Fig. 3 and Fig. 4.

1) As observed from Fig. 3 for the Gaussian, Adaptive Gaussian, and Weibull algorithms decomposing four sets of waveform samples, it has been shown that:

(a) After denoising, the Gaussian algorithms tends to generalize multiple superimposed peaks or several close peaks to individual peaks (see red box in Fig. 3(a3) and (a4)). In visual inspection, Multiple superimposed and mismatched waveform components with the original waveform also appear in Weibull (see red box in Fig. 3(c4)). However, in the case of continuous and narrow peaks, the Adaptive Gaussian accurately separates ten waveform components (see Fig. 3(b4)). This phenomenon indicates that the Adaptive Gaussian algorithm is highly capable of detecting the waveforms with multiple dense peaks.

(b) Both Adaptive Gaussian and Weibull algorithms decompose 1 or 2 more waveform components than the Gaussian algorithm does. For the first data set of waveforms, the 3rd waveform component of the Weibull algorithm is misjudged (see red box in Fig. 3 (c1)). This phenomenon shows that the accuracy of the Adaptive Gaussian algorithm is higher than that of the Weibull algorithm.

(c) The 2nd component of the Adaptive Gaussian algorithm is more like a complement to the 1st component (see red box in Fig. 3(b2)). The same phenomenon occurs as does with the Gaussian and Weibull algorithms. Retrieved by the Weibull algorithm, the 4th and 5th waveform components almost overlap

(see red box in Fig. 3(c4)). These cases reveal a fact that the Adaptive Gaussian and Weibull algorithms are prone to overfitting.

2) As observed from Fig. 4 for the RL, Gold deconvolution algorithms, and Gaussian algorithm, it can be seen from that:

(a) After the RL and Gold algorithms deconvolute the original waveform, a large change in pulse width and amplitude happens when compared to the original waveform (see solid red lines in Fig. 4(b2) and (c2)). This is indeed the result due to eliminating the impacts of the LiDAR system and output pulses. Therefore, the RL and Gold algorithms are able to improve the separability of waveform with multiple dense peaks.

(b) The Gold algorithm decomposes three waveform components, which is one less than the RL algorithm does (see red box in Fig. 4 (c1)). This phenomenon reveals that the Gold algorithm is inferior to the RL algorithm when dealing with simple waveforms.

(c) It was also noted that the RL and Gold algorithms amplify the noise amplitude as the number of the iteration increases. This phenomenon results in the formation of false peaks, as shown in the red boxes in Fig. 4 (b2) and (c2).
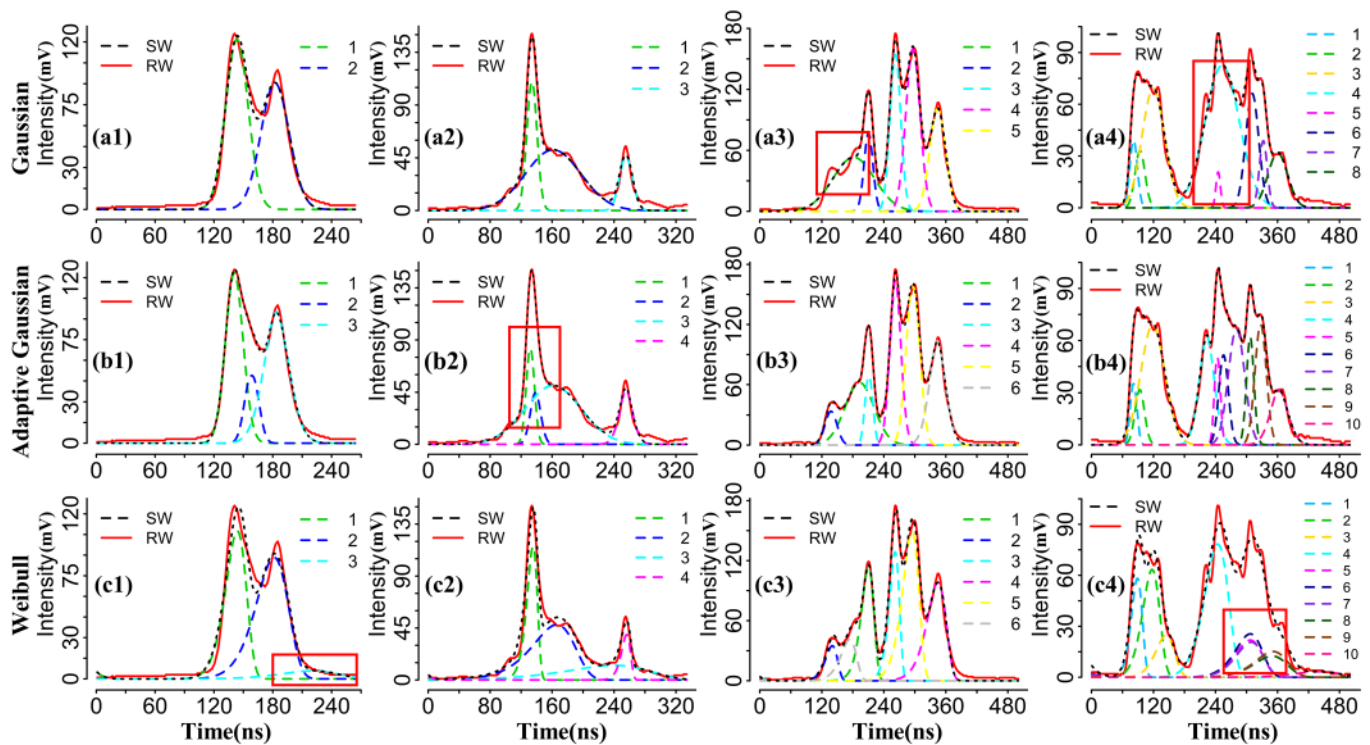

Fig. 3. Comparisons of the decomposition results with the Gaussian, Adaptive Gaussian, and Weibull algorithms for 4 waveform samples. The red solid line is the echo waveform. The black dashed line is the fitting waveform. The colored dashed lines are waveform components after decomposition.
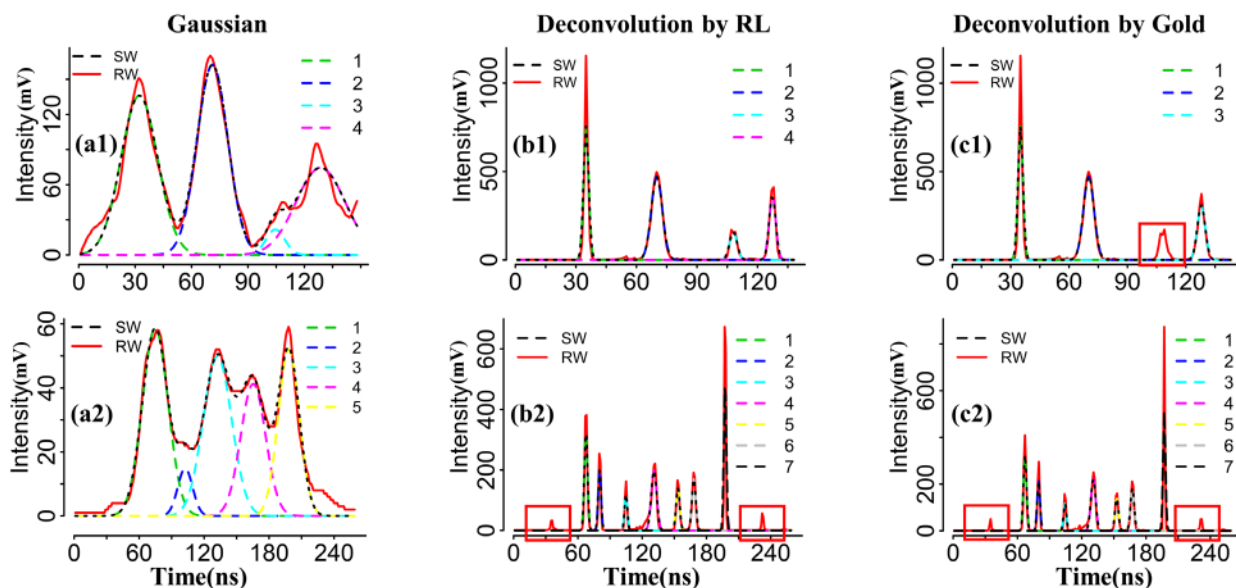

Fig. 4. Comparisons of the decomposition results with the Gaussian, RL, and Gold algorithms for 2 waveform samples. The red solid line is the echo waveform. The black dashed line is the fitting waveform. The colored dashed lines are waveform components after decomposition.

C. Comparison Analysis of the Accuracy of the Component Parameters

In addition, the parameters (peak A, peak location μ, pulse width σ, and shape parameter λ and k) describing a waveform component are selected to further analyze the characteristics of the five algorithms. The results are shown in Fig. 5 and Fig. 6.
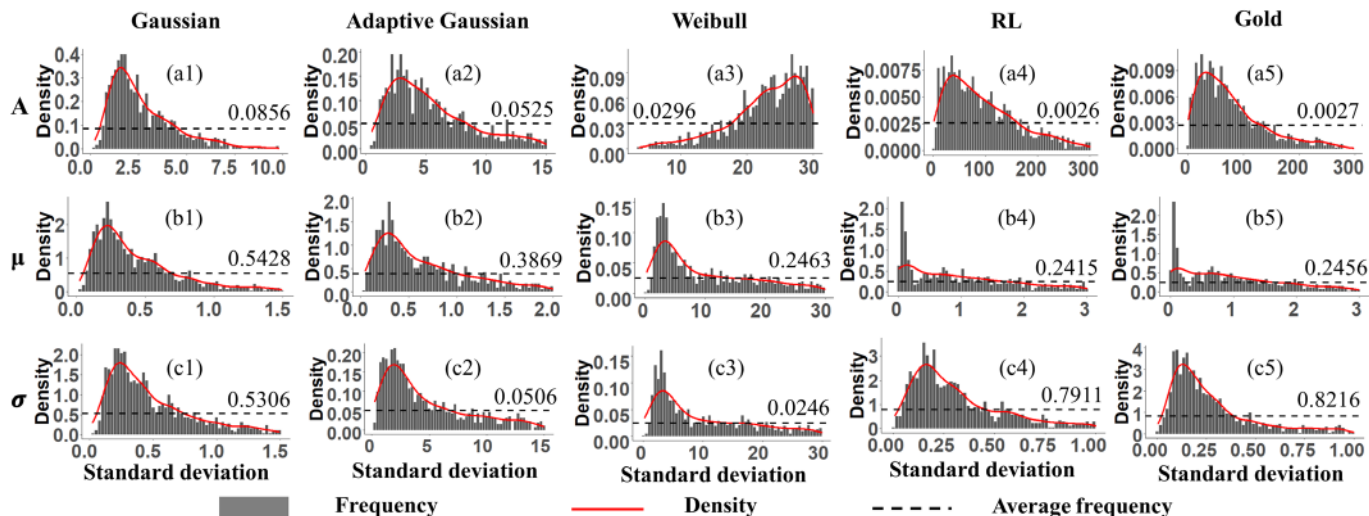

Fig. 5. Error comparison of three parameters A, μ, and σ among the five algorithms. The grey box is frequency. The red solid line is the density distribution. The black dashed line is the density mean value (data from Ogooué).
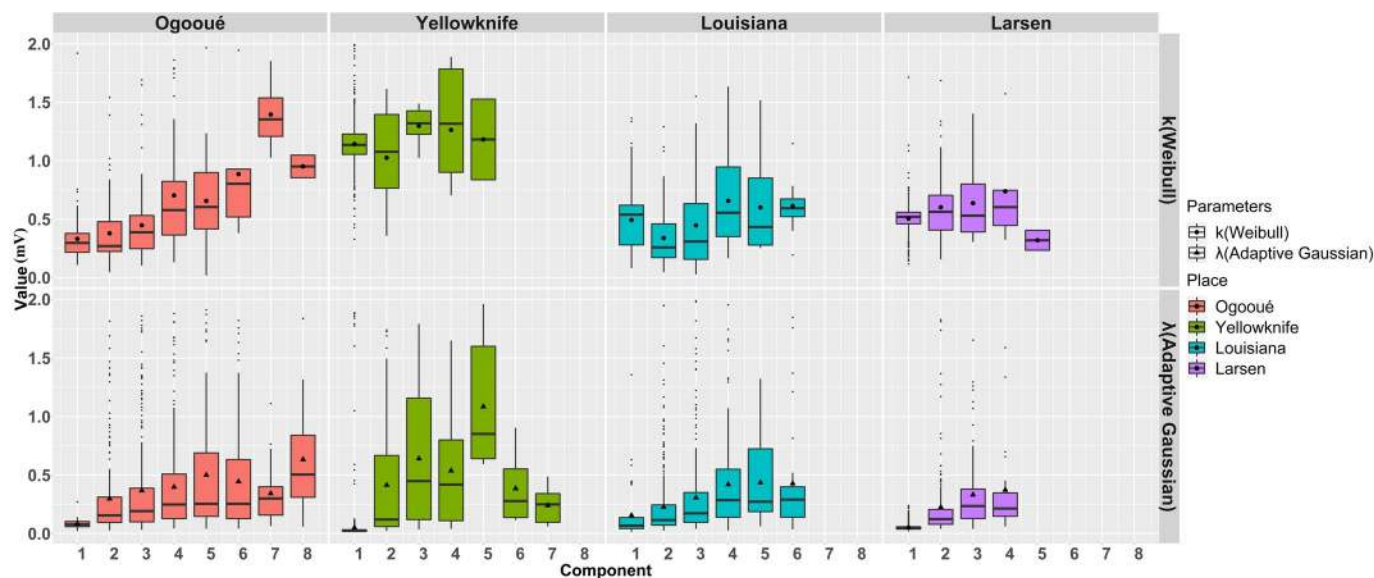

Fig. 6. Comparison of standard deviation for parameters λ and κ in the four experimental regions. λ and κ are the shape parameters for the Adaptive Gaussian and Weibull algorithms, respectively. The horizontal coordinate is the number of waveform components after a single waveform is decomposed.

1) Peak (A), peak position (μ), and pulse width (σ) are the three most basic parameters used as evaluating the characteristics of waveform components. The standard deviations of parameters for the five algorithms are shown in Fig. 5. It can be concluded that:

(a) The Gold and RL algorithms have the smallest standard deviation for the pulse width, which is lower than 0.25 mV. This result is due to the fact that the deconvolution eliminates the influence of the output pulse and the system impulse response, making the peaks of the RL and Gold algorithms easy to identify.

(b) The Gaussian and Adaptive Gaussian algorithms have the smallest standard deviation for the peak (lower than 10 mV) and the smallest standard deviation for the peak location (lower than 0.5 mV) out of the five algorithms. This fact demonstrates again that the two algorithms have the highest accuracy in the decomposed waveform components out of the five algorithms. However, the standard deviation of the 3 parameters of the Weibull algorithm is bigger than that from both Gaussian and Adaptive Gaussian algorithms. The result demonstrates that the advantages of the Weibull algorithm in processing asymmetric waveforms cannot be exploited when dealing with such waveforms that are similar to Gaussian distributed.

(c) The RL and Gold algorithms cause a big standard deviation of the peaks (concentrate between 0 and 100 mV) when compared with the other algorithms (also seen in Section B). As the amplitude greatly changes after deconvolution, this phenomenon does not mean that the RL and Gold algorithms are not capable in discriminating the peaks of waveforms.

2) Shape parameters λ in Adaptive Gaussian and k in Weibull are used to describe whether a waveform's shape is either flat or sharp. Both of standard deviations are calculated and the results are shown in Fig. 6. It can be concluded from Fig. 6 that:

(a) The standard deviation of the shape parameter λ is lower than 0.5, while the standard deviation of parameter k is higher than 0.5, i.e., the parameter λ has a higher precision than k does. Such a result implies that the Adaptive Gaussian algorithm has advantages over the Weibull algorithm.

(b) As observed from the experimental results from the four study areas, it is found that the parameter λ contains 122 more outliers than the parameter k does. This fact indicates that the Adaptive Gaussian algorithm appears bigger deviations in fitting the waveform than the Weibull algorithm does.

D. Comparison Analysis of Decomposition Accuracy

The root mean square error (*RMSE*), correlation coefficient (*C*), and fit superiority (R^2) are chosen as evaluation metrics to quantitatively assess the accuracy of the decomposition results [48]:

(1) *RMSE* refers to the square root of the difference between the fitted signal s_i' and the original signal s_i, and divided by the sampling numbers of signals. The computational formula is shown in Equation (9). *RMSE* can be used to measure the precision of an algorithm.

$$RMSE = \sqrt{\sum_{i=1}^{N}\left(s_i' - s_i\right)^2 \Big/ N} \qquad (9)$$

(2) *C* is the correlation coefficient between the fitted signal s_i' and the original signal s_i, which is used to measure the accuracy of an algorithm. It can be written as follows.

$$C = \sum_{i=1}^{N}\left(s_i' - \bar{s}'\right)^2\left(s_i' - \bar{s}\right)^2 \Big/ \sqrt{\sum_{i=1}^{N}\left(s_i' - \bar{s}'\right)^2\left(s_i' - \bar{s}\right)^2} \quad (10)$$

where $\bar{s}$ is the mean value of the original signal, $\bar{s}'$ is the mean of the fitted signal.

(3) R^2 is known as the goodness of fit, as shown in Equation (11). The closer R^2 is to 1, the better the effect is.

$$R^2 = 1 - \sum_{i=1}^{N}\left(s_i' - s_i\right)^2 \Big/ \sum_{i=1}^{N}\left(s_i' - \bar{s}\right)^2 \qquad (11)$$

where s_i' is the fitted signal, $\bar{s}$ is the mean value of the fitted signal, s_i is the original signal.

The results are shown in Table Ⅱ. It can be seen that:

1) The fitting error of the Gaussian algorithm is the biggest out of all algorithms, which reaches 9.96 mV, but the Gold algorithm has the smallest value at 4.802 mV. This fact reveals that the Gold algorithm has a strong robustness. In addition, it is also found from Table Ⅱ that the RL algorithm has an error of 7.424 mV, which is higher than the Gold algorithm has. This

is probably because the RL algorithm is more sensitive to noise than the Gold algorithm does.

2) Among the five algorithms, the correlation coefficient between the fitted waveform and original waveform of the Weibull algorithm is the lowest (0.710), while the Adaptive Gaussian algorithm has the highest correlation coefficient (0.851). This result indicates that the Adaptive Gaussian algorithm is effective in improving the accuracy of fitting complex waveforms.

3) The goodness of the fit for the five algorithms are all above 0.9 (close to 1), which means that all of the five algorithms have excellent fitting effects.

TABLE Ⅱ
COMPARISON OF DECOMPOSITION ACCURACY OF THE FIVE ALGORITHMS
(DATA: OGOOUÉ)

Algorithm	RMSE (mV)	C	R^2
Gaussian	**9.960**	0.814	0.954
Adaptive Gaussian	6.215	**0.851**	0.975
Weibull	9.637	**0.710**	0.941
RL	**7.424**	0.807	0.926
Gold	**4.802**	0.815	0.931

E. Comparison Analysis of Decomposition Speed

The LiDAR echo signals often contain hundreds of thousands or even millions of waveforms. Especially when data processing is requested in real-time mode, the processing speed is particularly important. Fig. 7 compares the processing speed of different algorithms. All experiments were conducted on the same computer: a Dell Vostro 3670-China HDD Protection with Windows 10 operating system. It is equipped with an Intel Core i5-8400 processor (2.80 GHz) and 8 GB RAM (Samsung DDR4 2400 MHz). It can be concluded that:

1) The difference of the processing speed can be ignored for the five algorithms when processing less than 10,000 pieces of data. However, the difference starts to become noticeable when the number of waveforms reaches tens of thousands. The threshold varies depending on the computing platform or hardware capability.

2) The RL algorithm consumes the most time in processing 100,000 pieces of data in the four regions at 18,000 seconds, 35,000 seconds, 40,000 seconds, and 35,000 seconds, respectively; the Weibull algorithm's processing speed decreases rapidly with increasing data, even surpassing the RL algorithm at 44,000 seconds in the Ogooué region. The results indicate that the Weibull and RL algorithms are not applicable to the LiDAR echo signals for the purpose of real-time computation.

3) The Gaussian algorithm consumes the least time for 100,000 pieces of data in the Louisiana and Ogooué regions, at 4,000 seconds and 7,000 seconds, respectively. However, the Gold algorithm consumes the least time for processing data for the Larsen Harbor and Yellowknife regions (1,000 and 2,000 seconds). Both algorithms have a fast signal decomposition speed.
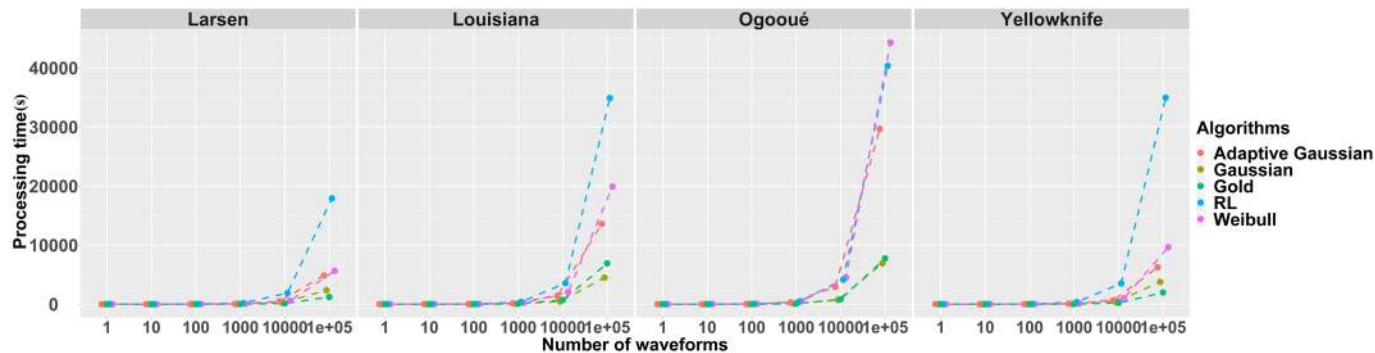
Fig. 7. The time consumed by five algorithms for waveform decomposition in different regions (Processing time varies with the number of waveforms, hardware, and other conditions).

F. Discussion

Through the experiments, it has been demonstrated that the Gaussian, Adaptive Gaussian, Weibull, and RL algorithms can effectively recomposite the waveform in the flat terrain. However, the Gold algorithm can display a strong capability for waveform decomposition in the forested areas, where multiple superimposed waves and weak echoes happen. The ability of the Gold algorithm to separate superimposed peaks is even better than predicted by Zhu et al [15]. In the study of Wagner et al., about 0.03% of the amplitude was negative for the Gaussian algorithm [42]. However, our experiments show that the Gold algorithm does not suffer from this problem. Moreover, the Gold algorithm can handle many noises. However, the Gold algorithm is not as good as the RL algorithm does in the area with less vegetations, such as Lassen area.

The RL algorithm is inferior to the Gold algorithm in Ogooué and Yellowknife areas where many hills and trees exist. In addition, "ringing effect" is also found in the RL and Gold algorithm, which is found by Wu et al. [19] in the Wiener Filter algorithm. The disadvantage of the RL algorithm is that the iterations are too many, whose conclusion is consistent with Wang et al. [25]. The performance of the RL algorithm is the best in the area of ice-covered Larsen Harbor.

The Weibull algorithm has a similar decomposing ability as the RL algorithm does in the ice-covered area, but the computation is time-consuming, despite no iteration. The Weibull algorithm also has a low accuracy in decomposition, which is in line with the findings of Zhou et al. [10]. The performances of the five algorithms are almost the same in the area of Yellowknife, where sparse trees and rocks are contained.

The experiment of Wagner et al. demonstrated that the Gaussian algorithm can fit 98% of the waveforms [42], but our experiments have further conclusions. The Gaussian algorithm is better at fitting waveforms with simple peaks, while it has the worst performance at fitting superimposed and weak waveforms. The parametric error analysis in Figure 5 shows that the Gaussian algorithm just lacks the ability to separate overlapping waveforms.

The deconvolution method outperforms the mathematical simulation method on the whole. The researched result from Parrish et al. [22] also demonstrated that the Expectation-Maximization deconvolution algorithm is better than the Gaussian algorithm.

With the findings above, it can be concluded that the selection of algorithms needs to be judged according to the real conditions. If the efficiency of data processing is very important, the Gaussian and Gold algorithms are the first choice; if many point clouds are expected to be generated from the original LiDAR point cloud data, mathematical simulation methods, such as Gaussian, are inferior to the RL and Gold deconvolution algorithms; if a study area with densely vegetations is encountered, the Gold algorithm is the first choice; if a study area with flat ice sheet, the RL algorithm has a better performance.

V. CONCLUSIONS

This paper compares the characteristics of five algorithms including Gaussian, Adaptive Gaussian, Weibull, RL, and Gold algorithms in processing LiDAR data covering four different regions. The four experimental regions include forests, glaciers, lakes, and residential objects respectively. The comparison analysis results in the following conclusions:

1) The fitting error of the Gaussian algorithm is as high as 9.96 mV; the false echo detection rate is 13.7% for Ogooué data; the number of decomposed components is the least in four data sets. Moreover, the Gaussian algorithm is easy to identify the superimposed or similar peaks as single peaks in general. The phenomena indicate that the performance of the Gaussian decomposition is strongly affected by the environment, and is far inferior to the other four algorithms when processing complex waveforms. However, the standard deviations of Gaussian parameters are lower than 0.5 mV, except the amplitude. These results show that the Gaussian algorithm lacks the ability to decompose complex waveforms, but has excellent accuracy for the decomposed components.

2) The number of waveform components decomposed by the Adaptive Gaussian and Weibull algorithms in Louisiana are 56.2k and 54.1k, respectively. Compared with the Gaussian algorithm (33.5k), the two algorithms have a strong ability to detect weak and superimposed waveforms. Besides, the position detection reveals that the Weibull algorithm separates many misinterpreted, superimposed, and overlapping waveforms. This phenomenon will unavoidably introduce large errors in the inversion of the objective distribution. The Adaptive Gaussian algorithm is able to decompose the waveform components with higher accuracy than the Weibull

This article has been accepted for publication in a future issue of this journal, but has not been fully edited. Content may change prior to final publication. Citation information: DOI 10.1109/JSTARS.2021.3096197, IEEE Journal of Selected Topics in Applied Earth Observations and Remote Sensing

> REPLACE THIS LINE WITH YOUR PAPER IDENTIFICATION NUMBER (DOUBLE-CLICK HERE TO EDIT) < 10

algorithm does. In the parameter analysis, the Adaptive Gaussian algorithm causes 122 more outliers than the Weibull algorithm does. These results above reveal that the Adaptive Gaussian and Weibull algorithms are prone to overfitting.

3) In the Louisiana data set, the number of waveform components decomposed by the RL and Gold algorithms (96.6k) is almost three times more than that of the Gaussian algorithm (33.5k), and two times more than that of the Adaptive Gaussian (56.2k) and Weibull (54.1k). The other experimental results also demonstrate that the two deconvolution algorithms, RL and Gold have advantages over the Gaussian, Adaptive Gaussian, and Weibull algorithms. Besides, both RL and Gold algorithms can effectively improve the separability of peaks. The false detection rates of the Gold algorithm are only 1.3%, 0.9%, 1.1%, and 0.1% in the four test regions, which can largely reduce the probability of detecting false waveform components.

4) The number of waveform components from the Gold algorithm is 12.9k, more than that from the RL algorithm in the forested Ogooué area. The Gold algorithm decomposes 2.6k less than the RL algorithm in the Larsen Harbor. The results indicate that the RL algorithm has better decomposition performance in the areas with less vegetations, while the Gold algorithm does for complex waveforms such as multiple, weak, and superimposed waveforms. The shortage of the RL algorithm is mainly in its convergence speed.

In conclusion, the Gaussian and Gold algorithms better meet the need for speed and stability in real-time computing, while the Adaptive Gaussian and Weibull algorithms are more likely to satisfy the need for the ability to decompose echo signals in densely vegetations or the ability to discriminate complex waveforms. With the comparison analysis for the characteristics of the five LiDAR waveform decomposition algorithms, these results and conclusions are helpful in promoting the applications of the different algorithms in various environments.

REFERENCES

[1] G. Zhou, C. Wang, M. Li, Y. Wang, S. Ye, and C. Han, "Advances and perspectives in bathymetry by airborne LiDAR," *International Conference on Intelligent Earth Observing & Applications 2015*, Vol. 9808, pp. 98082K, Dec. 2015, DOI: 10.1117/12.2207641.

[2] G. Zhou, C. Song, J. Simmers, and P. Cheng, "Urban 3D GIS From LiDAR and digital aerial images," *Computers & Geosciences*, vol. 30, no. 4, pp. 345-353, Aug. 2004, DOI: 10.1016/j.cageo.2003.08.012.

[3] G. Zhou, and X. Zhou, "Seamless Fusion of LiDAR and Aerial Imagery for Building Extraction," *IEEE Transactions on Geoscience and Remote Sensing*, Vol. 52, no. 11, pp. 7393-7407, 2014, DOI: 10.1109/TGRS.2014.2311991.

[4] S. Hancock, J. Armston, Z. Li, R. Gaulton, P. Lewis, M. Disney, and F. M. Danson, A. Strahler, C. Schaaf, K. Anderson, & K. J. Gaston, "Waveform LiDAR over vegetation: An evaluation of inversion methods for estimating return energy," *Remote Sensing of Environment*, Vol. 164, pp.208-224, 2015, DOI: 10.1016/j.rse.2015.04.013.

[5] G. Zhou, X. Zhou, Y. Song, D. Xie, L. Wang, G. Yan, …, & H. Wang, "Design of Supercontinuum Laser Hyperspectral LiDAR (SCLaHS LiDAR)," *International Journal of Remote Sensing*, 2021, Vol. 42, no. 10, pp. 3731–3755, https://doi.org/10.1080/01431161.2021.1880662.

[6] G. Zhou. "Urban High-Resolution Remote Sensing: Algorithms and Modelling," Taylor & Francis/CRC Press, USA: New York, 2020, pp.35-36.

[7] K. Wang, G. Liu, Q. Tao, L. Wang, and Y. Chen, "A Method for Solving LiDAR Waveform Decomposition Parameters Based on a Variable Projection Algorithm," *Complexity*, Vol. 2020, no. 5, pp. 1-13, 2020, DOI：10.1155/2020/6726139.

[8] M. A. Hofton, J. B. Minster, and J. B. Blair, "Decomposition of laser altimeter waveforms," *IEEE Transactions on geoscience and remote sensing*, Vol. 38 no. 4, pp. 1989-1996, 2000, DOI：10.1155/2020/6726139.

[9] J. Reitberger, P. Krzystek, and U. Stilla, "Analysis of full waveform LiDAR data for the classification of deciduous and coniferous trees," *International journal of remote sensing*, Vol. 29, no. 5, pp. 1407-1431, 2008, DOI：10.1080/01431160701736448.

[10] T. Zhou, and S. C. Popescu, "Bayesian decomposition of full waveform LiDAR data with uncertainty analysis," *Remote Sensing of Environment*, Vol. 200, pp. 43-62, 2017, http://dx.doi.org/10.1016/j.rse.2017.08.012.

[11] W. Wagner, A. Ullrich, V. Ducic, T. Melzer, and N. Studnicka, "Gaussian decomposition and calibration of a novel small-footprint full-waveform digitising airborne laser scanner," *ISPRS journal of Photogrammetry and Remote Sensing*, Vol. 60, pp. 2, pp. 100-112, 2006, DOI：10.1016/j.isprsjprs.2005.12.001.

[12] A. Chauve, C. Mallet, F. Bretar, S. Durrieu, M. P. Deseilligny, and W. Puech, "Processing full-waveform LiDAR data: modeling raw signals,"

International archives of photogrammetry, *Remote sensing and spatial information sciences*, pp. 102-107, Jul. 2008.

[13] M. Bruggisser, A. Roncat, M. E. Schaepman, and F. Morsdorf, "Retrieval of higher order statistical moments from full-waveform LiDAR data for tree species classification," *Remote sensing of environment*, Vol. 196, pp. 28-41, 2017. https://doi.org/10.1016/j.rse.2017.04.025.

[14] T. Zhou, S. C. Popescu, K. Krause, R. D. Sheridan, and E. Putman, "Gold–A novel deconvolution algorithm with optimization for waveform LiDAR processing," *ISPRS Journal of Photogrammetry and Remote Sensing*, Vol. 129, pp. 131-150, 2017, DOI：10.1016/j.isprsjprs.2017.04.021.

[15] R. Zhu, Y. Pang, Z. Zhang, and G. Xu, "Application of the deconvolution method in the processing of full-waveform LiDAR data," *In 2010 3rd International Congress on Image and Signal Processing*, Vol. 6, pp. 2975-2979, Oct. 2010, DOI：10.1109/CISP.2010.5646165.

[16] A. Roncat, G. Bergauer, and N. Pfeifer, "B-spline deconvolution for differential target cross-section determination in full-waveform laser scanning data," *ISPRS Journal of Photogrammetry and Remote Sensing*, Vol. 66, no. 4, pp. 418-428, 2011, DOI：10.1016/j.isprsjprs.2011.02.002.

[17] J. McGlinchy, J. A. Van Aardt, B. Erasmus, G. P. Asner, R. Mathieu, K. Wessels, ... and E. J. Ientilucci, "Extracting structural vegetation components from small-footprint waveform LiDAR for biomass estimation in savanna ecosystems," *IEEE Journal of Selected Topics in Applied Earth Observations and Remote Sensing*, Vol. 7, no. 2, pp. 480-490, 2013, DOI：10.1109/JSTARS.2013.2274761.

[18] B. Jutzi, and U. Stilla, "Range determination with waveform recording laser systems using a Wiener Filter," *ISPRS Journal of Photogrammetry and Remote Sensing*, Vol. 61, no. 2, pp. 95-107, 2006, DOI：10.1016/j.isprsjprs.2006.09.001.

[19] J. Wu, J. A. N. Van Aardt, and G. P. Asner, "A comparison of signal deconvolution algorithms based on small-footprint LiDAR waveform simulation," *IEEE Transactions on Geoscience and Remote Sensing*, Vol. 49, no. 6, pp. 2402-2414, 2011, DOI：10.1109/TGRS.2010.2103080.

[20] M. Azadbakht, C. S. Fraser, and K. Khoshelham, "A sparsity-based regularization approach for deconvolution of full-waveform airborne LiDAR data," *Remote Sensing*, Vol. 8, no. 8, pp. 648, 2016, DOI：10.3390/rs8080648.

[21] A. Jalobeanu, and G. Gonçalves, "Robust ground peak extraction with range error estimation using full-waveform LiDAR," *IEEE Geoscience and Remote Sensing Letters*, Vol. 11, no. 7, pp. 1190-1194, 2013, DOI：10.1109/LGRS.2013.2288152.

[22] C. E. Parrish, I. Jeong, R. D. Nowak, and R. B. Smith, "Empirical comparison of full-waveform LiDAR algorithms," *Photogrammetric Engineering & Remote Sensing*, Vol. 77, no. 8, pp. 825-838, 2011, DOI：10.14358/PERS.77.8.825.

[23] W. Wagner, A. Ullrich, T. Melzer, C. Briese, and K. Kraus, "From single-pulse to full-waveform airborne laser scanners: potential and practical challenges," *International Archives of the Photogrammetry, Remote Sensing and Spatial Information Sciences*, Vol. 35, pp. 201–206, Jan. 2004.

[24] Q. Z. Xiu, B. Z Jian, and G. Hong. "Comparison of wavelet transform and fourier self-deconvolution (FSD) and wavelet FSD for curve fitting," *The Analyst*, Vol. 125, no. 5, pp. 915-919, 2000, DOI：10.1039/b000064g.

[25] C. Wang, Q. Li, Y. Liu, G. Wu, P. Liu, and X. Ding, "A comparison of waveform processing algorithms for single-wavelength LiDAR bathymetry," *ISPRS Journal of Photogrammetry and Remote Sensing*, Vol. 101, pp. 22-35, 2015, DOI：10.1016/j.isprsjprs.2014.11.005.

[26] U. Soederman, A. Persson, J. Toepel, and S. Ahlberg, "On analysis and visualization of full-waveform airborne laser scanner data," *Laser Radar Technology and Applications X. International Society for Optics and Photonics*, Vol. 5791, pp. 184-192, May. 2005, DOI: 10.1117/12.604655.

[27] K. Cawse-Nicholson, J. van Aardt, S. Hagstrom, ..., and K. Krause, "Improving waveform LiDAR processing toward robust deconvolution of signals for improved structural assessments," in Proc. Laser Radar Technology and Applications XIX; and Atmospheric Propagation XI, Baltimore, Maryland, USA, 2014. pp. 90800I

[28] D. Gwenzi, and M. A. Lefsky, "Modeling canopy height in a savanna ecosystem using spaceborne LiDAR waveforms," *Remote sensing of environment*, Vol. 154, pp. 338-344, 2014, DOI：10.1016/j.rse.2013.11.024.

[29] Y. C Lin, J. P. Mills, and S. Smith-Voysey, "Rigorous pulse detection from full-waveform airborne laser scanning data," *International Journal of Remote Sensing*, Vol. 31, no. 5, pp. 1303-1324, 2010, https://doi.org/10.1080/01431160903380599.

[30] B. Hu, D. Gumerov, and J. Wang, "An integrated approach to generating accurate DTM from airborne full-waveform LiDAR data," *Remote sensing*, Vol. 9, no. 8, pp. 871, 2017, DOI：10.3390/rs9080871.

[31] C. Tison, J. M. Nicolas, F. Tupin, and H. Maître, "A new statistical model for Markovian classification of urban areas in high-resolution SAR images," *IEEE transactions on geoscience and remote sensing*, Vol. 42, no. 10, pp. 2046-2057, 2004, DOI：10.1109/TGRS.2004.834630.

[32] W. H. Richardson, "Bayesian-based iterative method of image restoration," *JoSA*, Vol. 62, no. 1, pp. 55-59, 1972, DOI：10.1364/JOSA.62.000055.

[33] D. S. Biggs, and M. Andrews, "Acceleration of iterative image restoration algorithms," *Applied optics*, Vol. 36, no. 8, pp. 1766-1775, 1997, DOI：10.1364/AO.36.001766.

[34] M. Morháč, V. Matoušek, and J. Kliman, "Efficient algorithm of multidimensional deconvolution and its application to nuclear data processing," *Digital Signal Processing*, Vol. 13, no. 1, pp. 144-171, 2003, DOI：10.1016/S1051-2004(02)00011-8.

[35] G. Zhou, and M. Xie, "Coastal 3-D morphological change analysis using LiDAR series data: a case study of Assateague Island National Seashore," *Journal of Coastal Research*, Vol. 25, no. 2, pp. 435-447, 2009, DOI：10.2112/07-0985.1.

[36] M. Morháč, J. Kliman, V. Matoušek, M. Veselský, and I. Turzo, "Efficient one-and two-dimensional gold deconvolution and its application to γ-ray spectra decomposition," *Nuclear Instruments and Methods in Physics Research Section A: Accelerators, Spectrometers, Detectors and Associated Equipment*, Vol. 401, no. 2, pp. 385-408, 1997, DOI：10.1016/S0168-9002(97)01058-9.

[37] R. W. Dirszowsky, and K. M. Wilson, "Biogeochemical evidence of eutrophication and metal contamination of frame lake, city of yellowknife, northwest territories, canada," *Environmental Earth Sciences*, Vol. 75, no. 1, pp. 1-13, 2016, DOI：10.1007/s12665-015-4852-2

[38] C. A. Silva, S. Saatchi, M. Garcia, N. Labriere, C. Klauberg, A. Ferraz, ... and A. T. Hudak, "Comparison of small-and large-footprint lidar characterization of tropical forest aboveground structure and biomass: A case study from central gabon," *IEEE Journal of Selected Topics in Applied Earth Observations and Remote Sensing*, Vol. 11, no. 10, pp. 3512-3526, 2018, DOI：10.1109/JSTARS.2018.2816962.

[39] V. Sarma. "Urban surface characterization using LiDAR and aerial imagery," Ph.D. dissertation, University of North Texas; USA, 2009.

[40] S. B. Simonsen, V. R. Barletta, R. Forsberg, and L. S. Sorensen, "Reconciled freshwater flux into the godthbsfjord system from satellite and airborne remote sensing," *International Journal of Remote Sensing*, Vol. 36, no. 1, pp. 361-374, 2015, DOI：10.1080/01431161.2014.995277.

[41] G. Zhou, and M. Xie, "GIS-based Three-dimensional Morphologic Analysis of Assateague Island National Seashore from LiDAR Series Datasets," *J. of Coastal Research*, vol. 25, no. 2, pp. 435–447, 2009.

[42] W. Wagner, A. Ullrich, V. Ducic, T. Melzer, and N. Studnicka, "Gaussian decomposition and calibration of a novel small-footprint full-waveform digitising airborne laser scanner," *ISPRS Journal of Photogrammetry and Remote Sensing*, Vol. 60, no. 2, pp. 100-112, DOI：10.1016/j.isprsjprs.2005.12.001

[43] C. Mallet, and F. Bretar, "Full-waveform topographic LiDAR: State-of-the-art," *ISPRS Journal of photogrammetry and remote sensing*, 2009, Vol. 64, no. 1, pp. 1-16, 2009, DOI：10.1016/j.isprsjprs.2008.09.007.

[44] G. Zhou, Z. Xiang, J. Yang, T. Yue, X. Nong, and O. Baysal, "Flash Lidar Sensor using Fiber Coupled APDs," *IEEE Sensors Journal*, vol. 15, no. 9, pp. 4758-4768, Sep. 2015, DOI：10.1109/JSEN.2015.2425414

[45] S. H. Long, G. Q. Zhou, H. Y. Wang, X. Zhou, J. L. Chen, and J. Gao, "Denoising of LiDAR Echo Signal Based on Wavelet Adaptive Threshold Method," *The International Archives of Photogrammetry, Remote Sensing and Spatial Information Sciences*, Vol. 42, pp. 215-220, 2020, DOI：10.1016/j.isprsjprs.2008.09.007.

[46] T. Zhou, and S. Popescu, "Waveformlidar: An R package for waveform LiDAR processing and analysis," *Remote Sensing*, Vol. 11, no. 21, pp. 2552, 2019, https://doi.org/10.3390/rs11212552.

[47] T. Zhou, and S. Popescu, "Waveformlidar: An R package for waveform LiDAR processing and analysis," *Remote Sensing*, Vol. 11, no. 21, pp. 2552, 2019, https://doi.org/10.3390/rs11212552.

[48] K. Guo, W. Xu, Y. Liu, X. He, and Z. Tian, "Gaussian half-wavelength progressive decomposition method for waveform processing of airborne laser bathymetry," *Remote Sensing*, Vol. 10, no. 1, pp. 35, 2018, DOI：10.3390/rs10010035.

Guoqing Zhou (SM'05) received the Ph.D. degree from Wuhan University, Wuhan, China, in 1994. He was a Visiting Scholar with the Department of Computer Science and Technology, Tsinghua University, Beijing, China, and a Post-Doctoral Researcher with the Institute of Information Science, Beijing Jiaotong University, Beijing. He continued his research as an Alexander von Humboldt Fellow with the Technical University of Berlin, Berlin, Germany, from 1996 to 1998, and was a Post-Doctoral Researcher with The Ohio State University, Columbus, OH, USA, from 1998 to 2000. He was an Assistant Professor, an Associate Professor, and a Full Professor with Old Dominion University, Norfolk, VA, USA, in 2000, 2005, and 2010, respectively. He has authored nine books, seven book chapters and more than 430 peer-refereed publications.

Shuhua Long is a M.S. student with the College of Geomatics and Geoinformation, Guilin University of Technology, Guilin, China. His research interests include algorithms for processing LiDAR data.